SPE-191623-MS

Coupled Fluid Flow and Geomechanical Modeling of Seismicity in the Azle Area North Texas

Rongqiang Chen, Xu Xue, Changqing Yao, Akhil Datta-Gupta, and Michael J. King, Texas A&M University; Peter Hennings and Robin Dommisse, University of Texas Bureau of Economic Geology

This paper was prepared for presentation at the 2018 SPE Annual Technical Conference and Exhibition held in Dallas, Texas, 24-26 September 2018.

Abstract

A series of earthquakes was recorded along a mapped fault system near Azle, Texas in 2013. To identify the mechanism of seismicity, coupled fluid flow and geomechanical simulation is carried out to model fluid injection/production and the potential onset of seismicity. Sensitivity studies for a broad range of reservoir and geomechanical parameters are performed and the calibrated models are used to identify controlling mechanisms for seismicity in the Azle area, North Texas and its relationship to hydrocarbon production and fluid injection in the vicinity. Geologic, production/injection, and seismicity data are gathered to build a detailed simulation model with coupled fluid flow and geomechanics. Geomechanical simulation results are used to calculate cumulative seismic moment magnitude. Sensitivity analyses for injection well head pressure and earthquake data are performed over a range of reservoir and geomechanical parameters. Influential parameters are selected to perform a pareto-based multi-objective history matching of well head pressures and seismic moments.

Geomechanical interaction has significant impact on seismicity in the Azle area. Unbalanced loading (overall injection and production) on different sides of the fault generates accumulation of strain change, resulting in the onset of seismicity. Previous studies seem to have significantly underestimated the fluid withdrawal rates, almost by an order of magnitude. The equivalent bottom-hole fluid rate used in this study suggests a drop in reservoir pore pressure which is consistent with the BHP trends. Thus, pore pressure increases may not explain the seismicity near the Azle area, as indicated in previous studies. Instead geomechanical effects and strain propagation to the basement appear to be the dominant mechanisms. The low fault cohesion and minimum horizontal stress obtained from history matching suggest that the faults must be near or at the critically-stressed state before the initiation of fluid production/injection. A sensitivity analysis indicates that the minimum horizontal stress and fracture gradient each play a critical role in the potential risk for seismicity related to fluid injection/production. Streamline flow pattern further proves that there is no fluid movement in the basement formation and the unbalanced loading from different sides of the fault is the controlling mechanism. This is the first study coupling fluid flow and geomechanics in the Azle area and the first to simultaneously calibrate the models with fluid flow and seismicity data.

Introduction and Background

Seismic events have been observed with increased frequence in the Fort Worth Basin since 2007. Several studies have been conducted to investigate the recent seismicity and many of them conclude that the main factors are the wastewater injection near the fault regions and reactivation of the faults (Frohlich et al. 2016, Frohlich et al. 2011, Gono et al. 2015, Hornbach et al. 2015). Hornbach et al. (2015) constructed a single phase flow model for the Ellenburger formation of the Azle area to simulate the pore pressure change and found the pore pressure increase near the faults could range from 0.01MPa to 0.14MPa. This pore pressure change could trigger the earthquake for near-critically stressed faults (Reasenberg and Simpson 1992, Stein 1999). However, Hornbach et al. (2015) only simulated the fluid flow in the Ellenburger formation and did not explicitly account for geomechanical effects and the resulting fault activation and seismic moment (Cappa and Rutqvist 2011, Jha and Juanes 2014, Park et al. 2016, Rutqvist et al. 2013, Segall and Lu 2015). Fan et al. (2016) conducted coupled fluid flow and geomechanics simulation to calculate the stress and pore pressure change along the faults during wastewater injection near Timpson, east Texas. Based on Mohr-Coulomb failure criteria, they showed the potential of fault activation associated with wastewater injection but they did not link the fault activation to the seismic moment magnitude. Previous studies either did not include the basement below the reservoir formation (Gono et al. 2015, Hornbach et al. 2015) or did not simulate the geomechanical effects in the basement although most large seismic events happened in the basement.

In the current study, we focus on the Azle area in North Texas, where a series of seismic events occurred between November 2013 and April 2014. To investigate the relationship between seismic events and field operations, we built a detailed simulation model with coupled fluid flow and geomechanics. This model consists of the overburden, the Marble Falls, the Barnett, the Ellenburger and the crystalline basement formation. Two conjugate faults are located based on earthquake catalog (USGS) and the main fault is extended to a depth of 8km, through the basement (Texas-RRC 2015). Two injection wells in the Ellenburger and 70 production wells in the Barnett are included in the model. The wastewater injection rate is from the H-10 form of the Railroad Commission of Texas website (Texas-RRC 2018) and the production rate is from the "DrillingInfo" data base. Our modeling includes multiphase effects accounting for both water and gas production, which results in substantial voidage under reservoir conditions. Pareto-based multi-objective optimization is conducted to calibrate the subsurface model using both the well head pressure data and the historical seismic events (Park et al. 2015). The Genetic algorithm (GA) is used in this optimization study, which is a stochastic approach that allows for uncertainty quantification for the model parameters by generating alternative plausible models rather than a unique deterministic solution. The overall workflow is shown in Fig. 1. To further validate the results from this workflow, a fine-scale Azle model with more than 2.7 million cells has also been constructed. Streamlines are traced on this fine-scale model to visualize the flow paths.

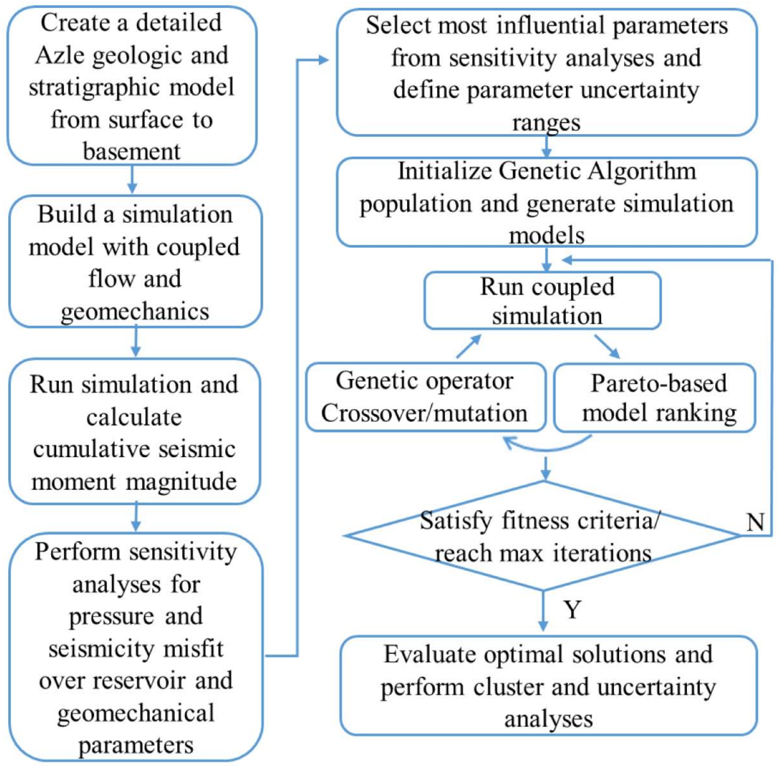

Figure 1—Workflow for Azle seismicity study using coupled flow and geomechanical modeling.

Geologic Model of the Azle Area

The Azle geologic model in this study is similar to the model used by Hornbach et al. (2015). The major difference is that we include the overburden as well as the basement, where most of the large seismic events have occurred. The model consists of two conjugate faults consistent with where most of the seismic events occurred. The primary normal fault extends down-dip through the crystalline basement (strike 225°, dip 60°~70°) (Hornbach et al. 2015).

Multi-stage hydraulic fracturing is routinely conducted in the Azle area to produce gas from the low permeability Barnett shale. The produced water, either originating from hydraulic fracture injection fluid or from the underlying Ellenburger formation, is reinjected into the Ellenburger formation through two injectors. The seismic events ($M_w \geq 2$) are shown in Fig. 2. From Fig. 2, the majority of the seismic events have occurred in the basement. The two conjugate faults are constructed based on the observed seismic events and previous geologic interpretation. The schematic 3D model is shown in Fig. 3. In this geologic model, uniform properties are used for each formation except at the fault locations. The reservoir and geomechanical properties for the base case are summarized in Table 1. The stress state and the Mohr-Coulomb failure envelope of the fault at the top of the basement are shown in Fig. 4, where we can see that the faults are near critically stressed since the initial stress state is very close to the Mohr-Coulomb failure envelope.

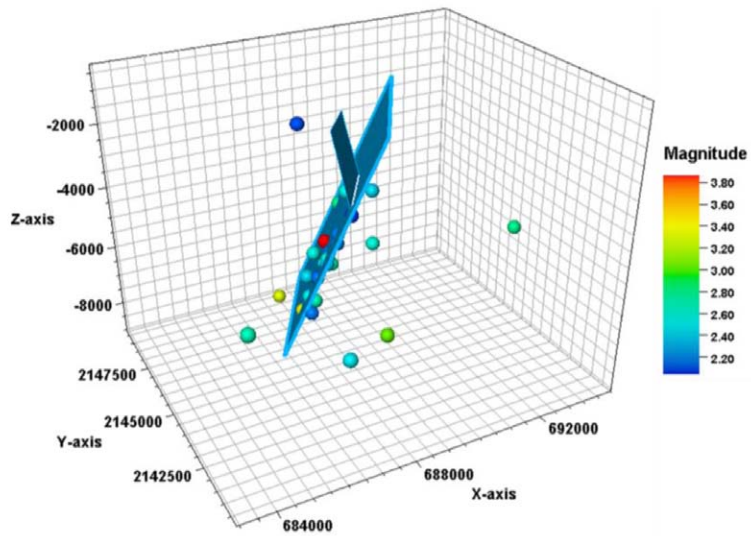

Figure 2—Azle area fault location and the locations of the earthquake events (Mw≥2).

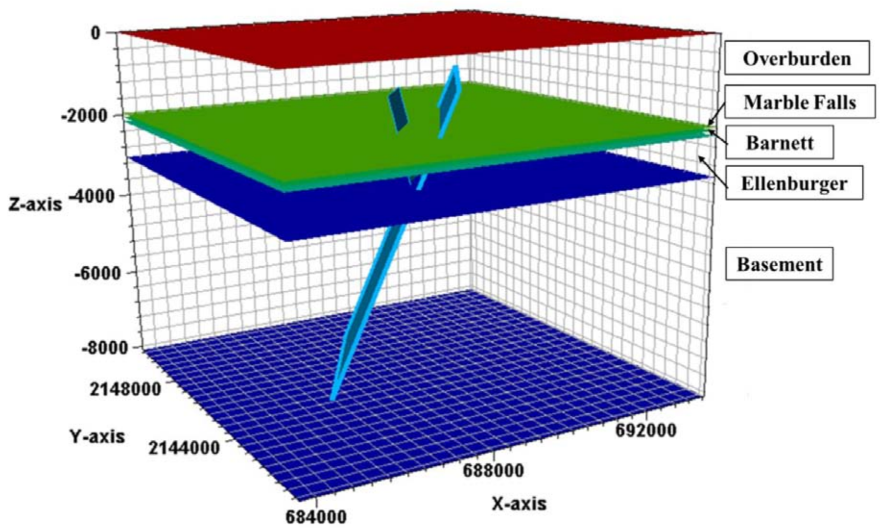

Figure 3—Azle geologic model with 2 conjugate faults.

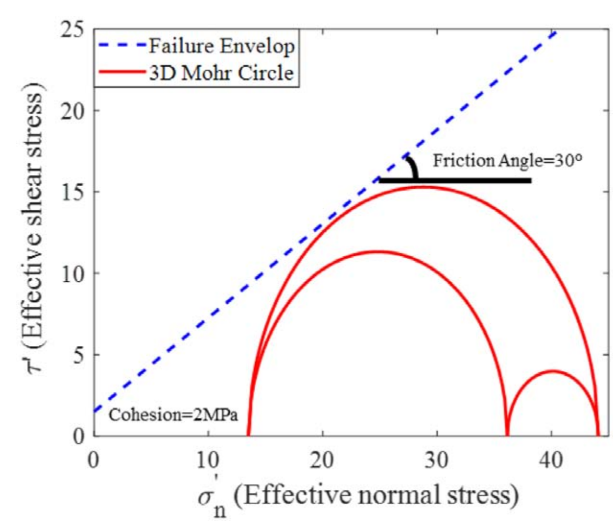

Figure 4—Initial stress state and the Mohr-Coulomb failure envelop for the base case.

Table 1—Reservoir and geomechanical properties for the Azle base case simulation model (Hornbach et al. 2015, Lund and Zoback 2016, Texas-RRC 2015, Wang 2000)

	Overburden	Marble Falls	Barnett	Ellenburger	Basement	Fault	Reference
Permeability (md)	190	0.01	1.00E-05	30	1.00E-04	1.00E-03	Hornbach et al. 2015
Porosity	0.2	0.2	0.06	0.055	0.05	Same as formation	
Pore Pressure	23082 kPa @ 2046 m						Texas-RRC 2015
Effective Vertical Stress Gradient	14.7 kPa/m						Snee and Zoback 2016
Effective Minimum Horizontal Stress Gradient	4.5 kPa/m						
$A_{\phi} = (s2-s3)/(s1-s3)$	0.74						
Direction of Horizontal Stress	N28.8E						
Young's Modulus (kPa)	1.44E+07	6.00E+07	4.00E+07	6.00E+07	4.30E+07	4.00E+07	Wang 2000
Poisson's Ratio	0.2	0.2	0.23	0.2	0.27	0.25	
Cohesion (kPa)	2.00E+04	2.00E+04	2.00E+04	2.00E+04	2.00E+04	1.00E+03	
Friction Angle (Deg)	30	30	30	30	30	30	

Coupled Flow, Geomechanical Modeling and the Seismicity Calculation

Our simulation model consists of 62×62×22 grid cells. The areal grid size is 160m by 160m and varying cell dimensions vertically with high resolution in the Barnett and Ellenburger as shown in Fig. 5. The model contains 1 layer for the overburden, 1 layer for the Marble Falls, 5 layers for the Barnett, 5 layers for the Ellenburger and 10 layers for the basement. The Barnett formation is the production zone and the Ellenburger is the wastewater injection zone. The two conjugate faults are represented as zig-zag faults in the model and have distinct properties from the reservoir. Two injection wells in the Ellenburger and 70 production wells in the Barnett are included in the model with total simulation time of 12 years.

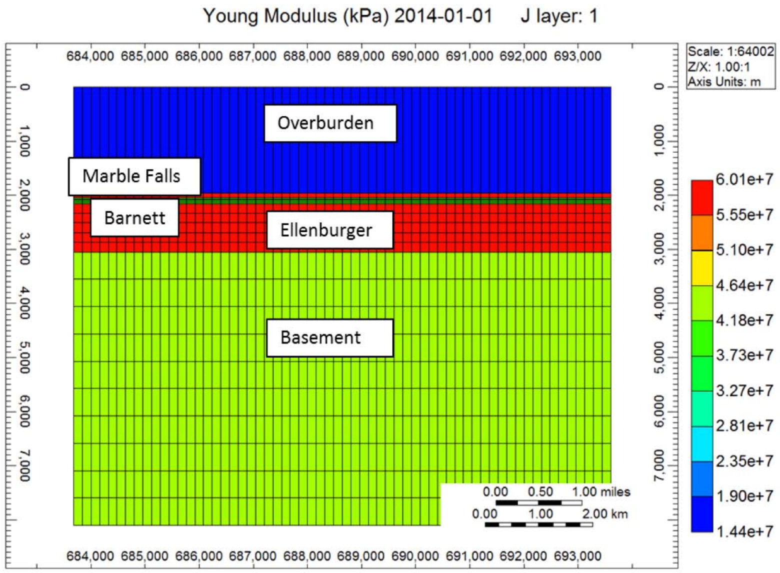

Figure 5—A cross-sectional view of the Azle simulation model. (Property visualized is the Young's modulus.)

We use CMG STARS (CMG 2018) as the forward simulator. CMG STARS couples fluid flow and reservoir deformation (geomechanics) together in a sequential manner. The fluid flow calculation first updates the pressure over a time interval; the geomechanical calculation updates the formation deformation in response to the new pressure and sends the new deformation back to the fluid flow calculation and the processes is repeated over other time intervals.

We calibrate our model with well head pressure and historical seismic events. The bottom-hole pressure (BHP) can be directly obtained from the simulator. The seismic moment magnitude is calculated from the geomechanical results. The seismic moment tensor is used to model the seismicity induced by fault activation and is calculated using the following equation (Aki and Richards 2002)

$$M_{pq} = \int_V c_{pqrs} \Delta e_{rs} dV \tag{1}$$

Here, C_{pqrs} is the stiffness tensor or the elastic modulus tensor and Δe_{rs} is the change of strain by deformation, which is obtained from the geomechanical simulation. The repeated indices indicate summation. We take the L_2 norm of the seismic moment tensor to obtain the intensity of the seismic moment, M_0 (Dahm and Krüger 2014)

$$M_0 = \left\| M_{pq} \right\|_{L_2} \tag{2}$$

The cumulative seismic moment magnitude is calculated as follows (Kanamori 1977)

$$M_w = \frac{\log M_0 - 16.1}{1.5} + 4.667 \tag{3}$$

By changing the reservoir properties, we calibrate our model to match the historical well head pressure and seismic events. The detailed steps and results are discussed in the following sections.

History Matching Using Multi-objective Optimization

We use the Pareto-based multi-objective history matching algorithm to calibrate the forward model with historical well head pressure and seismic events (Park et al. 2015). This methodology is suitable to minimize multiple (potentially conflicting) objective functions. Instead of aggregating different misfit functions, the pareto-based approach ranks the models based on the concept of dominance. Before history matching, we first conduct sensitivity studies for each type of data misfit, and then select the most influential parameters from the sensitivity analyses to perform the multi-objective history matching. We obtain multiple plausible parameter combinations that match reasonably well the historical bottom-hole pressure and seismic event data and then perform uncertainty analyses using the history matched models.

Pareto Optimization Background

Dominance relationship among different solutions forms the basis of the Pareto concept. For a minimization problem involving *n* objectives defined by objective functions *objn*, solution a dominates solution *b* if all objective functions represented by *a* are not greater than those of *b*, and at least one objective of a is strictly smaller than the corresponding objective of *b* (Han 2016).

The dominance concept can be graphically demonstrated in Fig. 6. For a 2-objective optimization problem, we have solution O shown in the red circle. We draw vertical and horizontal lines crossing solution O to divide the entire solution space into 4 regions. In region A, both *obj1* and *obj2* of all three solutions are smaller than those of solution O. Thus, solutions in region A are better solutions and dominate solution O. Both *obj1* and *obj2* of solutions in region D are larger than those of solution O, so solutions in region D are dominated by solution O. In region B and D, solutions have one objective smaller but the other objective larger than that of solution O. Thus, there is no dominance relationship between region B and D solutions and solution O.

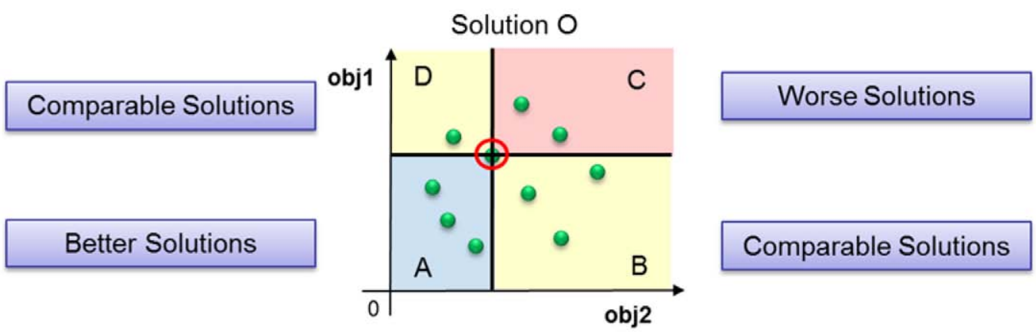

Figure 6—Dominance concept demonstrated using solution O.

Similar exercise can be performed on every solution to obtain the overall ranking of the solutions. In Fig. 7, a set of solutions which are not dominated by any other solutions are classified as rank 1 solutions. Then, rank 1 solutions are excluded from the solution space, and the same exercise is performed in the remaining solution space to obtain rank 2 solutions. Then, both rank 1 and rank 2 are excluded to obtain the next rank level of non-dominated solutions. The process is continued until all solutions are assigned a rank level. The solution ranking exhibits the following features: (i) solutions on the same rank (same Pareto front) are equally optimal, (ii) the lower rank solutions are more competitive than the higher rank ones for a minimization problem, and (iii) trade-offs of the front reveal potential conflict between objectives.

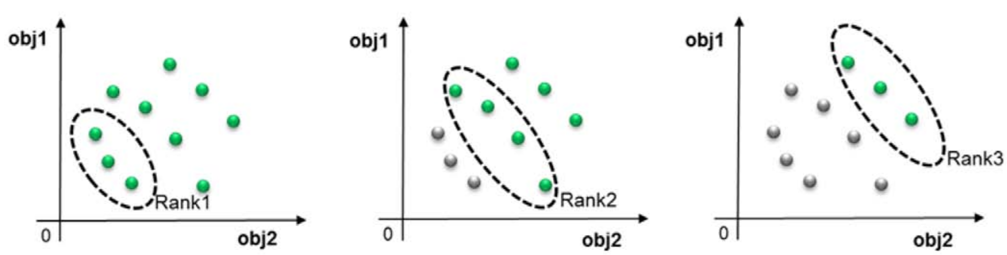

Figure 7—Solution ranking demonstration.

Genetic Algorithm Background

We use the genetic algorithm, one of the evolutionary algorithms, for model calibration. The genetic algorithm imitates biological principles of evolution - survival of the fittest. It has been extensively applied to history matching problems (Bittencourt and Horne 1997, Romero and Carter 2001, Yin et al. 2011). The evolution starts from a population of randomly generated individuals. In each generation, the fitness of every individual (the rank of every model parameter set in our study) in the population is evaluated. Multiple individuals are stochastically selected from the current population (based on their fitness), and modified (recombined and possibly randomly mutated) to form a new population. The new population is then used in the next iteration of the algorithm. Commonly, the algorithm terminates when either the maximum number of generations is produced or a satisfactory fitness level is reached (Yin et al. 2011). Thus, multiple plausible parameter combinations are generated with low rank level matching reasonably well with historical data. In this study, we have 2 objective functions to minimize for model calibration: (i) bottom-hole pressure (BHP) misfit and (ii) seismic moment magnitude misfit.

BHP Misfit

The injector BHP misfit is calculated using the following equation:

$$obj_{BHP} = \log\left(\sum_{j=1}^{Nwell} \sqrt{\sum_{i=1}^{Ntime} (BHP_{i,j}^{obs} - BHP_{i,j}^{cal})^2}\right) \quad (4)$$

Here, N_{well} is the total number of history matching wells, N_{time} is the total number of pressure data observation times, the superscript *obs* indicates the observed data, and the superscript *cal* indicates the calculated value from the simulation.

Seismic Moment Magnitude Misfit

Three simulations are used in Fig. 8 to demonstrate the seismic moment magnitude misfit calculations. The magnitude misfit is the vertical difference between cumulative seismic moment magnitude and the observed seismic event magnitude at the observed time and is given by:

$$obj_{magnitude} = \sqrt{\sum_{i=1}^{Nevent} (Mw_i^{obs} - Mw_i^{cal})^2} \quad (5)$$

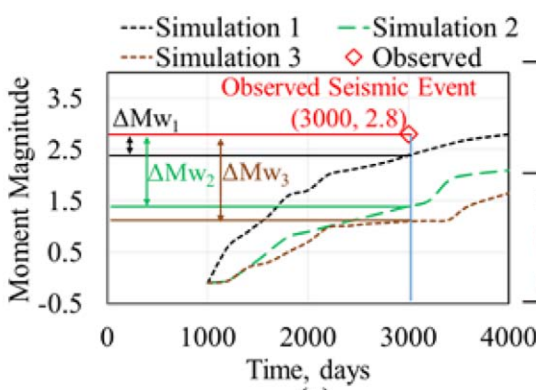

(a)

	Mw @3000 days	ΔMw
Simulation 1	2.4	0.4
Simulation 2	1.4	1.4
Simulation 3	1.2	1.6

(b)

Figure 8—An illustration of the calculation of the seismic moment magnitude misfit (a) seismic moment magnitude evolution (b) seismic moment magnitude misfit calculation.

Here, N_{event} is the total number of history matching seismic events, Mw_i^{obs} is the observed seismic moment magnitude of event *i*, and Mw_i^{cal} is the calculated cumulative seismic moment magnitude from the simulation within a specified search radius of seismic event *i*. The search radius represents the uncertainty in the spatial location of the seismic event.

It is important to note that the intent here is not to predict when an earthquake will occur and the calculated cumulative seismic moment magnitude does not suggest an equal-magnitude earthquake. Instead, the calculated cumulative seismic moment magnitude implies the maximum stored energy from plastic strain change and whether the accumulated energy is sufficient to cause a corresponding seismic event.

Sensitivity Analysis

Fig. 9 shows the calculated sensitivity of the injector bottom-hole pressure misfit to different parameters. The flow parameters viz. permeability anisotropy and permeability and the geomechanical properties viz.the Young's Modulus and Poisson's ratio are the most influential parameters, particularly for the Ellenburger formation. This is because the two injectors are completed within the Ellenburger formation. The injector bottom-hole pressure is not sensitive to the parameters other than from the Ellenburger. From the sensitivity analysis, permeability anisotropy, Ellenburger permeability, Young's modulus, and Poisson's ratio are identified as the primary tuning parameters for BHP calibration.

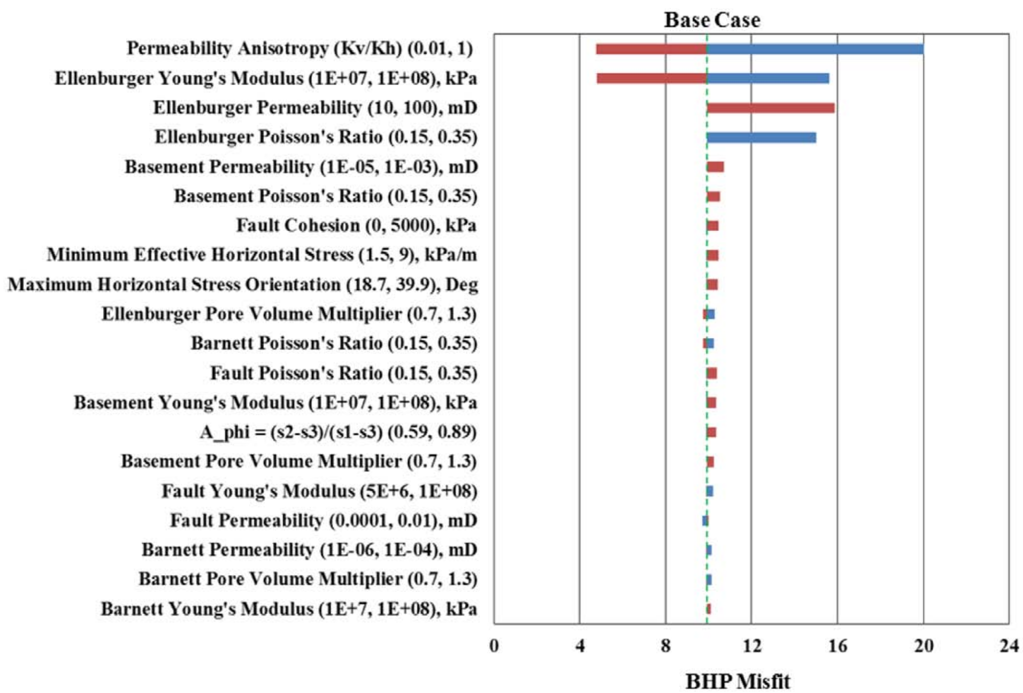

Figure 9—Sensitivity of the injector bottom-hole pressure misfit to various reservoir/geomechanical parameters.

Fig. 10 shows the sensitivity of the cumulative seismic moment magnitude misfit to different parameters. Minimum effective horizontal stress and fault cohesion are the most sensitive parameters since they directly determine the initial stress state of the faults based on the Mohr-Coulomb criteria. Fault Poisson's ratio is also sensitive since this parameter is directly used in the seismic moment magnitude calculation in Eq. (1).

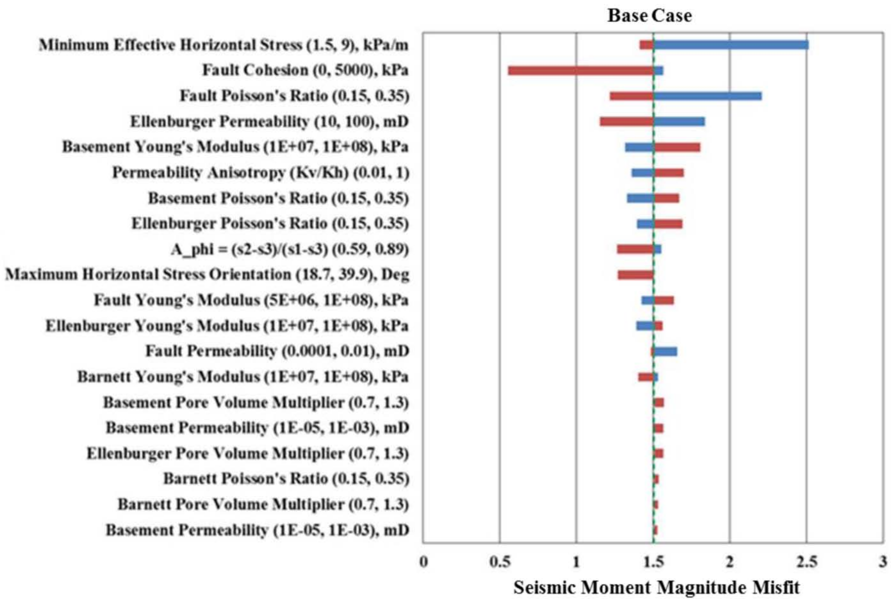

Figure 10—Sensitivity of the cumulative seismic moment magnitude misfit to various reservoir/geomechanical parameters.

Pareto-based Multi-objective History Matching and Uncertainty Analysis

Table 2 gives the primary tuning parameters and their ranges for the history matching process. Most of the geomechanical properties have high uncertainty ranges because of limited data or prior knowledge. Fig. 11a shows the trade-off between seismic moment magnitude and BHP misfit using the pareto-based multi-objective history matching. Comparing generation 5 with generation 1, we can clearly see generation 5 moves towards the bottom left of the figure, which indicates misfit reduction of the two objective functions. Also, we can see a clear 'Pareto front' between BHP and seismic magnitude misfits in generation 5. Fig. 11b shows the seismic moment magnitude matching. The initial generation response is scattered while the rank 1 matches are moving toward the unit slope line. Fig. 11c & Fig. 11d show the BHP matching of the two injectors. All the rank 1 models show good agreement with historical pressure data, which slowly declines over the injection period.

Table 2—History matching parameters and ranges.

	Description	Parameter	Base	Low	High
Geomechanical Properties	Ellenburger Young's Modulus (kPa)	YOUNGE	6.00E+07	1.00E+07	1.00E+08
	Basement Young's Modulus (kPa)	YOUNGB	4.30E+07	1.00E+07	1.00E+08
	Fault Young's Modulus (kPa)	YOUNGF	4.00E+07	1.00E+07	1.00E+08
	Fault Cohesion (kPa)	COHEF	1000	0	5000
	Ellenburger Poisson's Ratio	POISSE	0.27	0.2	0.35
	Fault Poisson's Ratio	POISSF	0.25	0.2	0.35
	Minimum Horizontal Stress (kPa/m)	Shmin	4.5	1.5	9
Reservoir Properties	Ellenburger Pore Volume Multiplier	PVE	1	0.7	1.3
	Ellenburger Permeability Multiplier	PERME	1	0.1	10
	Permeability Anisotropy	Kv/Kh	0.1	0.01	0.2

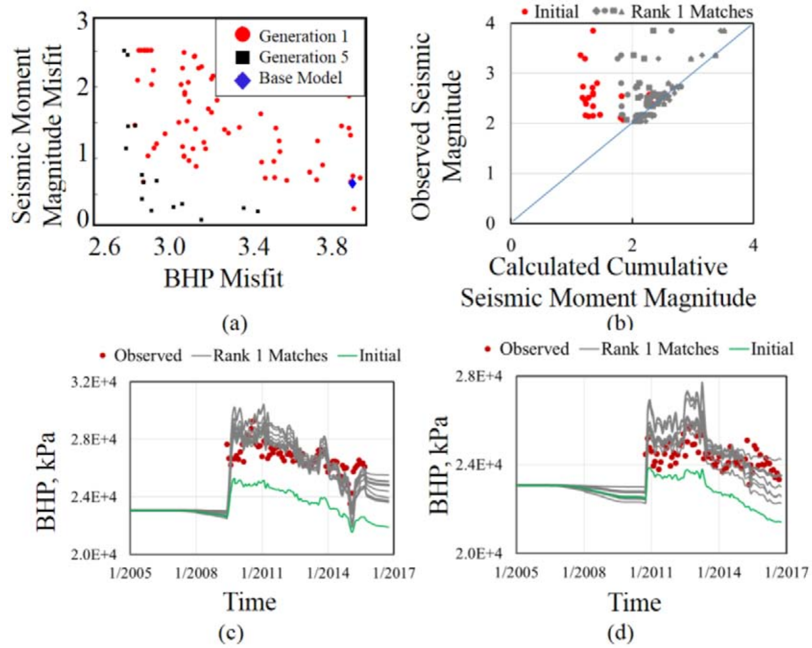

Figure 11—Multi-objective history matching results (a) Trade-off between seismic moment magnitude and BHP misfit (b) seismic moment magnitude match (c) Injector 1 pressure match (d) Injector 2 pressure match.

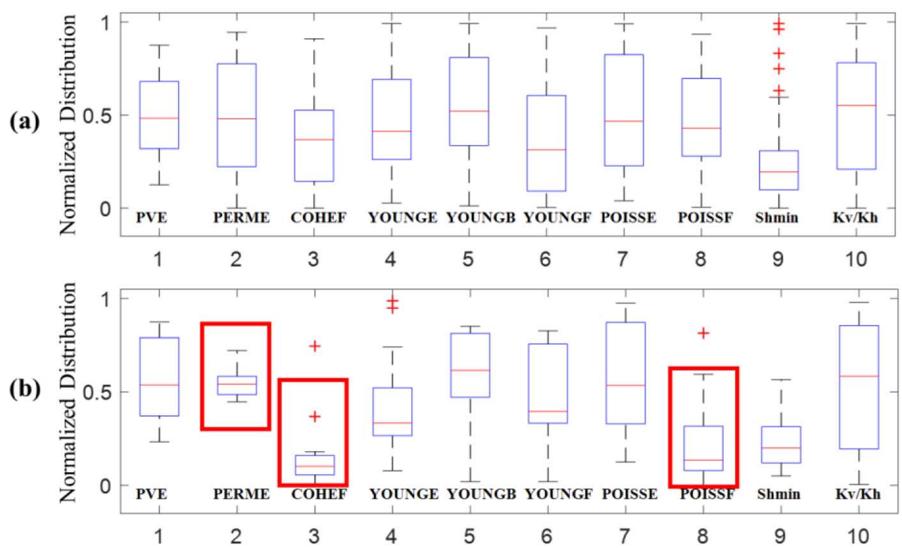

Figure 12—History match parameter ranges (a) prior distribution (b) posterior distribution.

Fig. 12 gives boxplots of the prior and posterior distribution of the history match parameters. From the result, we can clearly see significant reduction of uncertainty ranges for several key parameters, especifically the Ellenburger permeability (#2 PERME), fault cohesion (#3 COHEF), and fault Poisson's ratio (#8 POISSF). There is also uncertainty range reduction for several other geomechanical parameters. One interesting phenomenon is that both fault cohesion (#3 COHEF) and the minimum horizontal stress (#9 Shmin) move towards lower bounds, indicating the two conjugate faults are actually in a critically-stressed state before the start of injection.

Fig. 13 shows classification tree analysis of seismic moment magnitude and BHP misfit. The history matched models have been grouped into four classes: the best fit being in class 1 and the worst fit are in class 4. The classification tree is generated by recursively finding the variable splits that best separate the output into groups where a single category dominates (Breiman et al. 1984). The algorithm searches through the variables one by one to find the optimal split within each variable and the splits are compared among all variables to find the best split for that fork. The process is repeated until all groups contain a single category. Thus, the more dominant variables are generally the splits closer to the tree root. From Fig. 13, the most important parameters for the seismic moment magnitude misfit are the minimum horizontal stress (Shmin) and fault Poisson's ratio (POISSF) and for the BHP misfit it is the Ellenburger permeability (PERME).

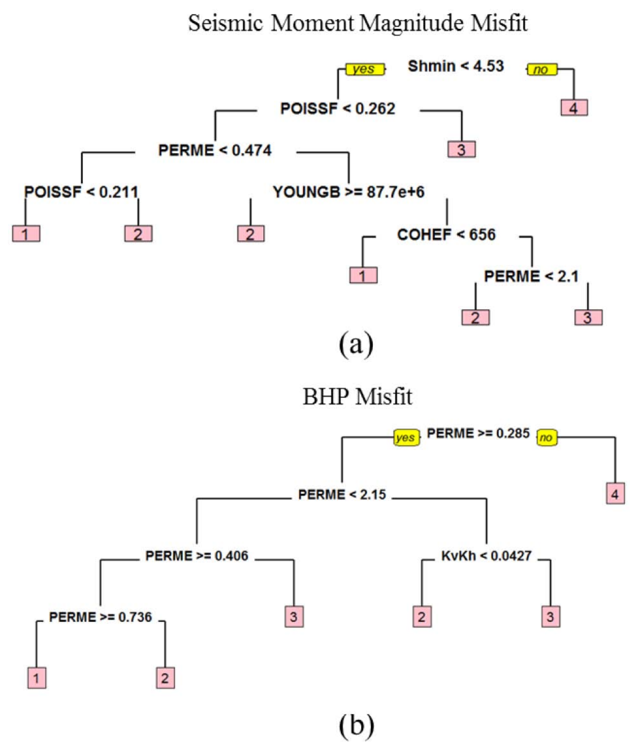

Figure 13—Parameter importance analysis using classification tree (a) seismic moment magnitude misfit (b) injector pressure misfit.

It is important to note that if the minimum horizontal stress is higher than a threshold value (4.53 kPa/m), all simulation results will have an insufficient accumulation of seismic moment magnitude and fall into class 4, indicating that they significantly deviate from the seismic event history. The minimum horizontal stress gradient is essentially the formation fracture gradient often obtained from minifrac tests. Thus, one way to evaluate whether there is a risk of seismicity is to identify those depths in formations with low fracture gradient.

In addition to classification tree analysis, we utilize entropy (mutual information) analysis to quantitatively evaluate the strength of different input-output association (Mishra 2009). The mutual information between x and y, which measures the reduction in uncertainty of y due to knowledge of x is defined as (Bonnlander and Weigend 1994)

$$I(x, y) = \sum_i \sum_j P_{ij} \ln \frac{P_{ij}}{P_i P_j} \tag{6}$$

Here, P_{ij} is the probability of outcomes corresponding to both state x_i and state y_j, while P_i is the probability of outcomes corresponding to state x_i alone, and P_j is the probability of outcomes corresponding to state y_j alone. A useful measure of importance defined on the basis of mutual information is called the R-statistic (Granger and Lin 1994)

$$R^2(x,y) = 1 - \exp\left(-2I(x,y)\right) \tag{7}$$

R takes values in the range of [0,1], with values increasing with I(x,y). R is zero if x and y are independent, and is unity if there is an exact linear relationship between x and y.

Fig. 14 shows the strength of different input-output associations quantitatively. As expected, reservoir properties such as Ellenburger permeability (PERME), Ellenburger Young's modulus (YOUNGE), and permeability anisotropy (Kv/Kh) have the strongest impacts on injector pressure. For seismic moment magnitude, Shmin is the most influential parameter but POISSF and Kv/Kh are almost equally influential. Thus, the classification tree analysis and the entropy analysis complement each other in this study. While the entropy analysis provides the absolute strength of entire input-output associations, the classification tree analysis offers useful insights into what variables are most important in determining whether the outputs fall into each specific category.

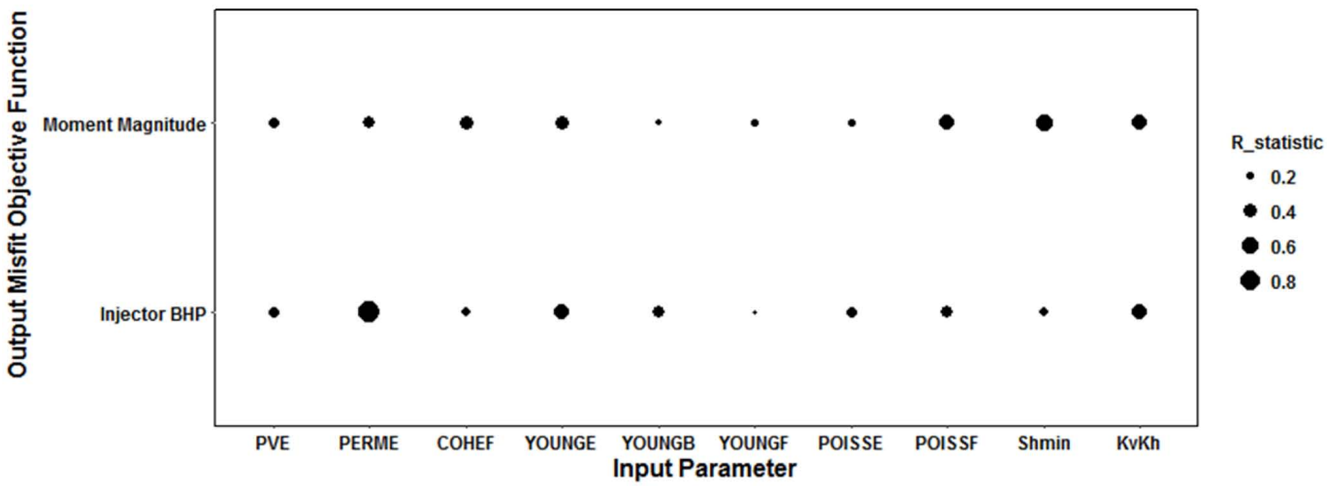

Figure 14—Bubble plot showing quantitative strength of different input-output association.

Unbalanced Loading

Wastewater disposal is often associated with induced seismicity and much of the literature has focused on reservoir pore pressure increase after injection as the primary mechanism for the seismicity (Hornbach et al. 2015, Hornbach et al. 2016). Our results indicate that these effects may not be the primary reason for the seismic events at Azle. First, the pressure change is larger in the Ellenburger formation but most of the Mw≥2 seismic events were actually recorded in the basement. Second, there is sufficient evidence suggesting that the Barnett and Ellenburger formations are not isolated and the amount of fluid volume extracted from the reservoir may easily offset the amount of water injected. Thus, we do not see a pressure increase in the Ellenburger and the basement formations, and this result agrees with the observed well BHP trends. Third, using the fault permeability value from Hornbach et al. (2015), there is no pressure change in the basement (Fig. 15a) and the streamline distribution in Fig. 15b shows that the majority of the fluid movement occurs in the Ellenburger and Barnett formation with no fluid movement in the basement. However, we can see the displacement for the weaker elements with low cohesion value in the basement as shown in Fig. 16.

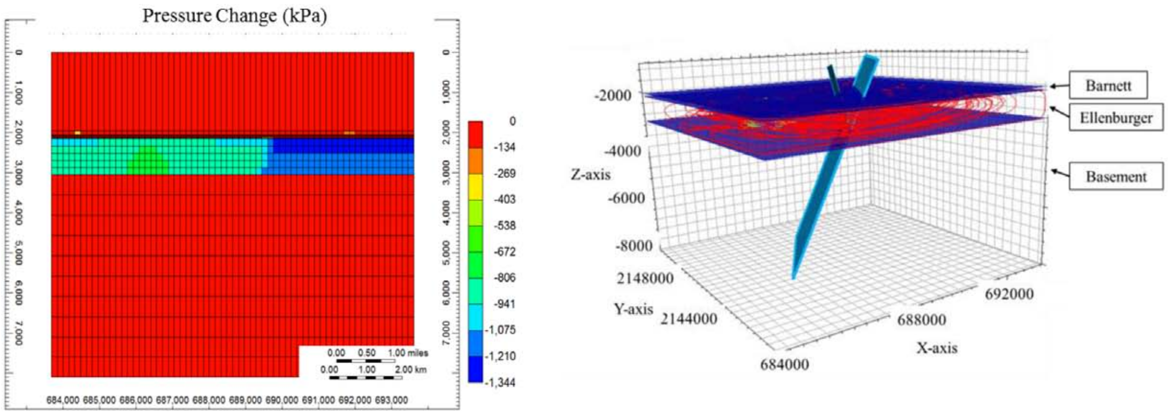

(a) (b)

Figure 15—Matched case (a) pressure change and (b) streamline trajectory at the time of the observed seismic event.

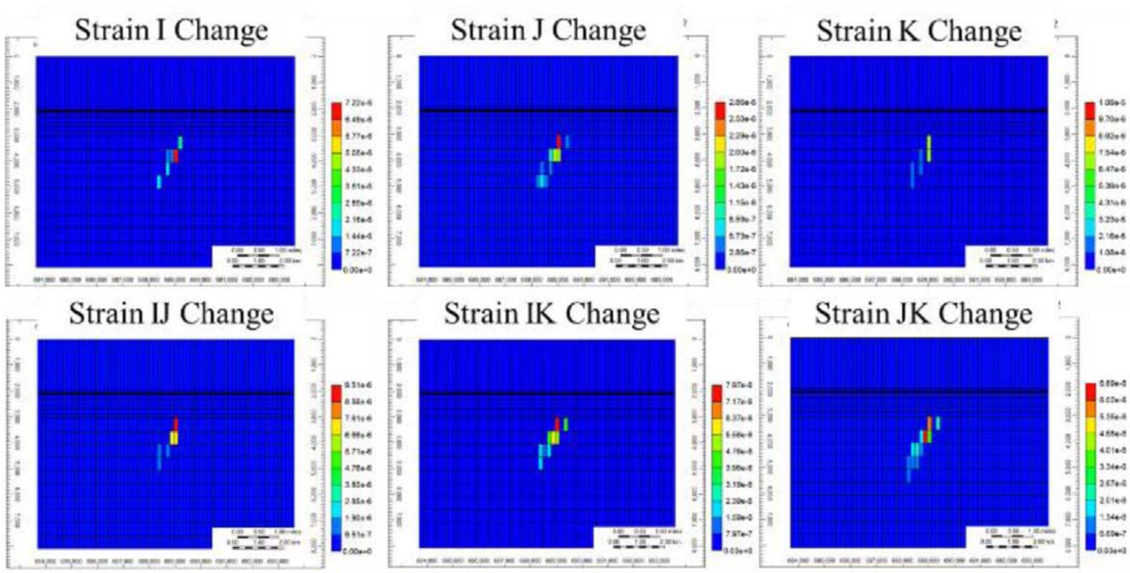

Figure 16—Matched case strain component changes at the time of the observed seismic event.

Even with no pore pressure change, the geomechanical interaction at the weaker elements of the basement formation are able to accumulate enough plasticity strain to match the observed seismic event magnitude. The accumulation of strain change is caused by the unbalanced loading on different sides of the fault as shown in Fig. 17. On the northwest side of the main fault, there are 2 injectors and approximately 20 producers. The overall net reservoir volume of fluids (cumulative injection volume minus cumulative production volume) at the end of simulation history is approximately 3.5E6 m^3. On the other side of the fault, there are approximately 50 producers and no injector. The overall net reservoir volume of fluids is approximately -8.1E6 m^3. The unbalanced fluid loading can be more easily visualized using streamlines. Streamlines are traced from both injectors and producers, with each streamline from either producer or injector carrying an equal amount of fluid volume. Fig. 17c clearly shows that the northwest side of the main fault has less concentration of streamlines than the southeast side, indicating less production, and the 2 injectors on the northwest side further increase the load imbalance. Even though the reservoir is not completely compartmentalized by the fault, the difference of net reservoir volume change on different sides of the fault creates an unbalanced loading to the basement, leading to the onset of seismicity.

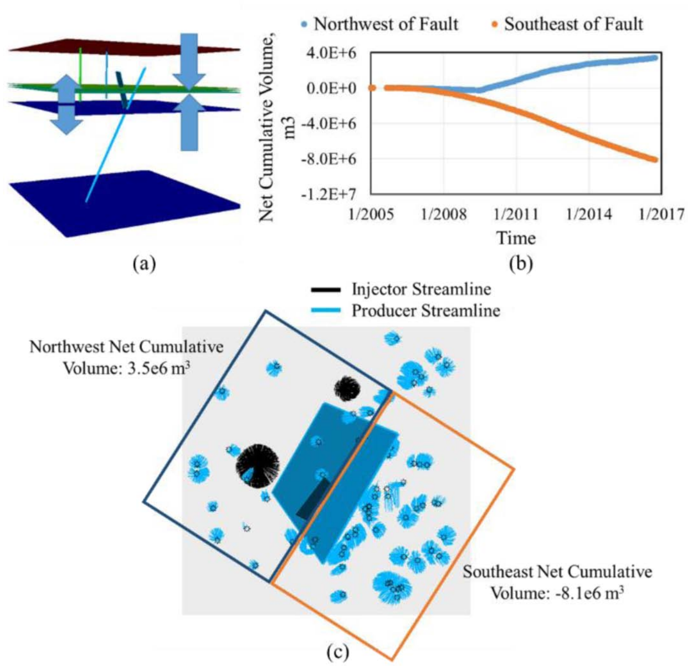

Figure 17—Unbalanced fluid loading in the basement generates accumulation of strain change, leading to potential onset of seismicity: (a) schematic diagram of loading, (b) net cumulative volume on different sides of the fault, and (c) top view injector and producer streamline distribution.

Streamline and Flow Visualization at the Fine-scale Model

In order to further validate our history matched results and the unbalanced loading evaluated using the coarse-scale Azle model, a fine-scale Azle model with more than 2.7 million cells has been constructed. The calibrated properties from the coarse-scale Azle model are used to tune the fine-scale geologic model and streamlines are traced to visualize the flow paths. The injector-producer flow pattern is analyzed to validate the identified controlling mechanism from the coarse-scale simulation results.

Fine-Scale Geologic Model

A high-resolution subsurface geologic model of the Azle area is shown in Fig. 18. This high resolution geologic model has been constructed in the Petrel Geomodeling tool (Schlumberger 2018) for application to the geomechanical assessment of fault reactivation and seismicity. The domain of the model is a 144 km^2 area in NW Tarrant County, NE Parker County, and southern Wise County. The model consists of stratigraphic control surfaces and through-going normal faults that have been interpreted in a 3D structural framework following the general workflow outlined in Krantz and Neely (2016). Approximately 2,000 vertical and horizontal wells from the general region were used to constrain the stratigraphic surfaces in the model (top Lower Barnett formation at ~1,830 m SSTVD, top of Ellenburger formation ~1,920 m SSTVD, and top of igneous and metamorphic basement at ~2,900 m SSTVD). Faults in the region were constrained by an integration of stratigraphic mapping, structural interpretation, earthquake hypocenters (Hornbach et al. 2015), and review of existing publications and public records from the Texas Rail Road Commission. There are three NE-striking normal faults in the model that are in close proximity to the earthquakes: Azle (6.5 km long, 50 m throw at the top of the Ellenburger formation), Azle Antithetic (3.0 km long, 60 m throw), and Reno (3.4 km long, 40 m throw). These faults are part of the Llano Fault System in the Fort Worth Basin as described by Ewing (1991). The lateral extent, strike, and general dip of the faults was constrained by 3D interpretation and earthquake hypocenter location. The petrophysical interpretation of porosity and permeability for the stratigraphic units in the model was conducted by analysis of 14 wells in the vicinity for which triple combo digital well log suites are available. Porosity was calculated using neutron-density cross plot techniques and a permeability index was derived using porosity to permeability transforms described in Lucia (2007). Total water saturation was calculated using an Archie equation. The calculated petrophysical attributes from the wells were distributed throughout the model using both sequential Gaussian simulation and moving average techniques.

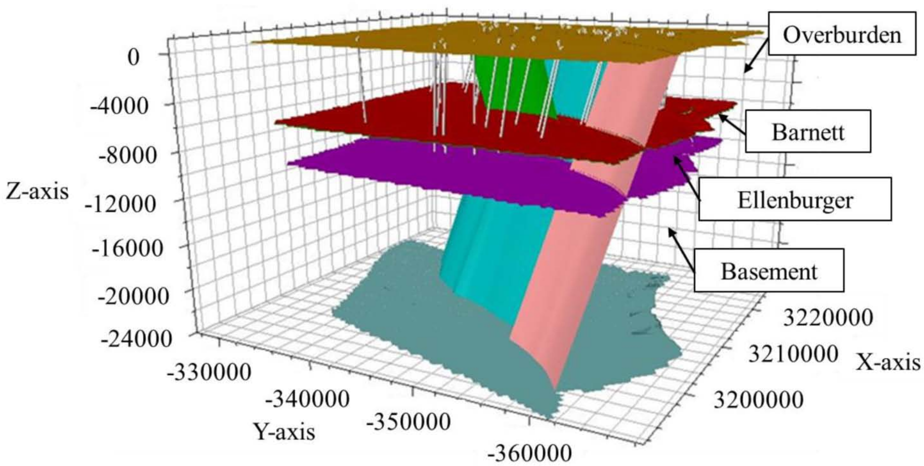

Figure 18—Azle fine-scale geologic model

Streamline Tracing

The Azle fine scale geologic model results in a faulted corner point grid representation of the subsurface, where the geometry of the grid cells conforms to the structural description of the faults and the stratigraphy of the geologic description. Flow simulation is performed in this model to examine the mechanisms already discussed, but now with this more detailed reservoir description. To visualize flow paths and the relationships between injectors and producers, streamline tracing was used as a simulation post-processing tool, conducted by an in-house code. Streamlines are traced using total fluid flux which can be used to track the overall movement of fluids in the reservoir, providing a convenient way for visualizing the impact of reservoir heterogeneity on fluid flow. The fundamental parameter in streamline tracing is time of flight (τ), which is defined as the travel time of a neutral tracer along the streamlines. In this study, streamline tracing is implemented based on time of flight computation proposed by Jimenez et al. (2007), simplifying the process by a parameterization of the streamline trajectories using a time-like parameter T, called the pseudo-time of flight, that increases along the streamlines,

$$dT = \frac{d\tau}{\phi \cdot J(\alpha,\beta,\gamma)} = \frac{d\alpha}{Q_1(\alpha)} = \frac{d\beta}{Q_2(\beta)} = \frac{d\gamma}{Q_3(\gamma)} \tag{8}$$

Here, α, β, and γ are dimensionless (isoparametric) coordinates across each corner point cell crossed by a streamline, and the Jacobian $j(\alpha, \beta, \gamma)$ represents local volume along the streamline. This set of equations can be integrated explicitly and independently for each direction to obtain streamline trajectories. Instead of working with velocity, the volumetric flux is used and is replaced by its linear interpolant in each direction. The integral solution in the α-direction is

$$\int_0^{T_E} dT = \int_{\alpha_0}^{\alpha} \frac{d\alpha}{Q_1(\alpha)} = \int_{\alpha_0}^{\alpha} \frac{d\alpha}{a_1 + c_1 \cdot \alpha} = \frac{1}{c_1} \ln[\frac{a_1 + c_1 \cdot \alpha}{a_1 + c_1 \cdot \alpha_0}] \tag{9}$$

Identical constructions will arise when integrating in the β- and γ- directions. The pseudo-time for the transit of neutral tracer across a cell will be given by the minimum pseudo-time of flight over allowable edges (Jimenez et al. 2007),

$$\Delta T = Min\,Positive\left(\Delta T_{x1},\Delta T_{x2},\Delta T_{y1},\Delta T_{y2},\Delta T_{z1},\Delta T_{z2}\right) \tag{10}$$

Once the pseudo-time of flight T is known, the exit coordinate of the particle is easily calculated using the general solution of Eq. (9) in all three directions and solving for each unit coordinate.

$$\alpha_e = \alpha_0 + \left(a_1 + \alpha_0 c_1\right)\left(\frac{e^{c_1 T} - 1}{c_1}\right) \tag{11}$$

Knowing the unit space coordinates (α, β, γ) in Eq. (11), we can use tri-linear interpolation to transform the unit coordinates to the physical space (x, y, z) (Datta-Gupta and King 2007). After obtaining their solution, we can determine τ from the integral:

$$\tau = \phi \int_0^T J\left(\alpha(T),\beta(T),\gamma(T)\right) dT \tag{12}$$

Fig. 19a shows the streamlines distribution after 10 years of production, where light blue lines are for producers and dark blue lines are for injectors. It is clear that wastewater injected through injectors will not transport to the southeast side of the main fault and also there are more streamlines from producers on the northwest side of the main fault, consistent with unbalanced loading on different sides of the main fault. From Fig. 19b, we can see that there is no streamline in the basement, indicating there is no volumetric flux or pressure change in the basement, consistent with the results from the calibrated coarse scale model.

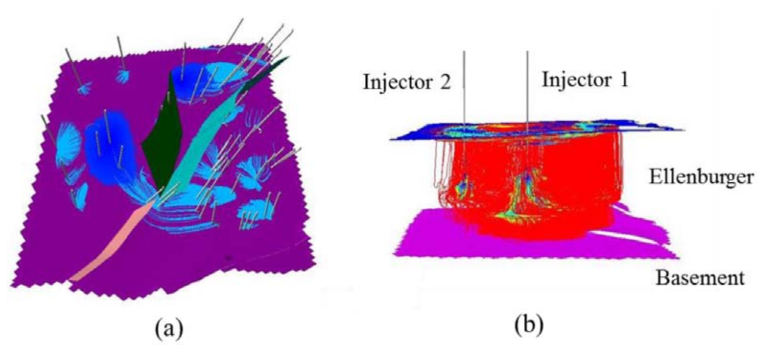

Figure 19—(a) Horizontal view of streamlines from producers and injectors (10000 days cut-off) (b) vertical view of streamlines from producers and injectors

Fig. 20 shows the pressure distribution along streamlines after 10 years of production. We can see that there is a pressure difference between the two sides of the main fault, which results in the unbalanced loading on the basement to cause the onset of seismicity at the weaker elements of the basement.

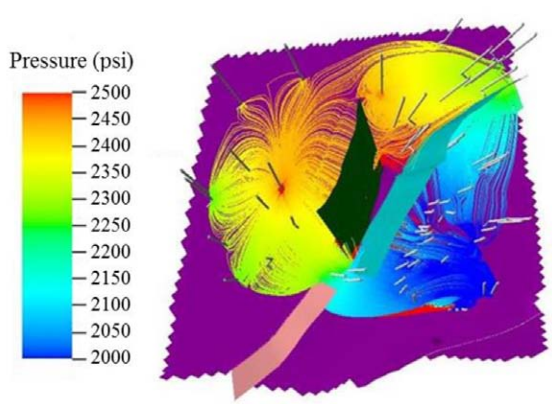

Figure 20—Pressure distribution along streamlines

Conclusion

1. Geomechanical interactions have significant impact on the seismicity observed in the Azle area, North Texas. Unbalanced loading on different sides of the fault in the basement generates accumulation of strain change, leading to the onset of seismicity.
2. Unlike previous studies, our results indicate that pore pressure changes may not be sufficient to explain the seismicity near the Azle area. Previous studies have significantly underestimated the fluid withdrawal rates, almost by an order of magnitude. The equivalent bottom-hole fluid rate (reservoir voidage from water and gas production) used in this study suggests a reduction in reservoir pore pressure which is consistent with the observed well head pressure trends.
3. The low values of fault cohesion and minimum horizontal stress inferred from history matching seem to indicate that the faults were near or at the critically-stress state before the initiation of fluid production/injection. Also, a parameter importance analysis using classification tree shows that the minimum horizontal stress/fracture gradient play a critical role in evaluating the potential risk of seismicity.
4. Fine-scale modelling with streamline tracing further validates the unbalanced loading concept in the Azle area. The amount of the unbalanced loading on different sides of the main fault can be clearly visualized from streamline distribution and the lack of streamlines in the basement again demonstrates the lack of fluid flux in the basement formation.

Acknowledgements

The authors would like to acknowledge financial support from members of the Texas A&M University Joint Industry Project, MCERI (Model Calibration and Efficient Reservoir Imaging) and Bureau of Economic Geology Project, TexNet Seismic Monitoring Program. The authors thank Schlumberger for use of the Petrel Geological Modeling software and IHS Markit for access to well data.

Reference

Aki, K. and Richards, P. G. 2002. *Quantitative Seismology*: University Science Books.

Bittencourt, A. C. and Horne, R. N. 1997. Reservoir Development and Design Optimization. Paper SPE-38895-MS. Proc., SPE Annual Technical Conference and Exhibition.

Bonnlander, B. V. and Weigend, A. S. 1994. Selecting Input Variables Using Mutual Information and Nonparametric Density Estimation. *Proc., International Symposium on Artificial Neural Networks*.

Breiman, L., Friedman, J., Stone, C. J. et al. 1984. *Classification and Regression Trees*: Taylor & Francis.

Cappa, F. and Rutqvist, J. 2011. Modeling of Coupled Deformation and Permeability Evolution During Fault Reactivation Induced by Deep Underground Injection of CO2. *International Journal of Greenhouse Gas Control* **5** (2): 336—346.

CMG. 2018. *CMG STAR Manual*, https://www.cmgl.ca/stars.

Dahm, T. and Krüger, F. 2014. Moment Tensor Inversion and Moment Tensor Interpretation. In *New Manual of Seismological Observatory Practice Deutsches GeoforschungZentrum GFZ*.

Datta-Gupta, A. and King, M. J. 2007. *Streamline Simulation: Theory And Practice*: Society of Petroleum Engineers.

Ewing, T. E. 1991. *The Tectonic Framework of Texas: Bureau of Economic Geology*, University of Texas at Austin.

Fan, Z., Eichhubl, P., and Gale, J. F. W. 2016. Geomechanical Analysis of Fluid Injection and Seismic Fault Slip for the Mw4. 8 Timpson, Texas, Earthquake Sequence. *Journal of Geophysical Research: Solid Earth* **121** (4): 2798—2812.

Frohlich, C., DeShon, H., Stump, B. et al. 2016. A Historical Review of Induced Earthquakes in Texas. *Seismological Research Letters* **87** (4): 1022—1038.

Frohlich, C., Hayward, C., Stump, B. et al. 2011. The Dallas-Fort Worth Earthquake Sequence: October 2008 Through May 2009. *Bulletin of the Seismological Society of America* **101** (1): 327—340.

Gono, V., Olson, J. E., and Gale, J. F. 2015. Understanding the Correlation between Induced Seismicity and Wastewater Injection in the Fort Worth Basin. Proc., 49th US Rock Mechanics/Geomechanics Symposium, San Francisco, California.

Granger, C. and Lin, J. 1994. Using the Mutual Information Coefficient to Identify Lags in Nonlinear Models. *Journal of Time Series Analysis* **15** (4): 371—384.

Han, J. 2016. *Multiobjective and Level Set Methods for Reservoir Characterization and Optimization*. Ph.D. Dissertation, Texas A&M University.

Hornbach, M. J., DeShon, H. R., Ellsworth, W. L. et al. 2015. Causal Factors for Seismicity Near Azle, Texas. *Nature Communications* **6**: 6728.

Hornbach, M. J., Jones, M., Scales, M. et al. 2016. Ellenburger Wastewater Injection and Seismicity in North Texas. *Physics of the Earth and Planetary Interiors* **261** (Part A): 54–68.

Jha, B. and Juanes, R. 2014. Coupled Multiphase Flow and Poromechanics: A Computational Model of Pore Pressure Effects on Fault Slip and Earthquake Triggering. *Water Resources Research* **50** (5): 3776—3808.

Jimenez, E., Sabir, K., Datta-Gupta, A. et al. 2007. Spatial Error and Convergence in Streamline Simulation. *SPE Reservoir Evaluation & Engineering* **10** (3): 221—232.

Kanamori, H. 1977. The Energy Release in Great Earthquakes. *Journal of Geophysical Research* **82** (20): 2981—2987.

Krantz, B. and Neely, T. 2016. Subsurface Structural Interpretation: The Significance of 3-D Structural Frameworks. In *3-D Structural Interpretation: Earth, Mind, and Machine*. American Association of Petroleum Geologists.

Lucia, F. J. 2007. *Carbonate Reservoir Characterization: An Integrated Approach*: Springer Science & Business Media.

Lund, S. J. and Zoback, M. D. 2016. State of Stress in Texas: Implications for Induced Seismicity. *Geophysical Research Letters* **43** (19): 10,208–214.

Mishra, S. 2009. Uncertainty and Sensitivity Analysis Techniques for Hydrologic Modeling. *Journal of Hydroinformatics* **11** (3-4): 282–296.

Park, H. Y., Datta-Gupta, A., and King, M. J. 2015. Handling Conflicting Multiple Objectives Using Pareto-Based Evolutionary Algorithm During History Matching of Reservoir Performance. *Journal of Petroleum Science and Engineering* **125**: 48–66.

Park, J., Kim, J., and Zhu, D. 2016. Assessment of Potential Fault Activation in Tarim Basin During Hydraulic Fracturing Operations by Using Rigorous Simulation of Coupled Flow and Geomechanics. Paper SPE-181811-MS. Proc., SPE Asia Pacific Hydraulic Fracturing Conference.

Reasenberg, P. A. and Simpson, R. W. 1992. Response of Regional Seismicity to the Static Stress Change Produced by the Loma Prieta Earthquake. *Science* **255** (5052): 1687—1690.

Romero, C. E. and Carter, J. N. 2001. Using Genetic Algorithms for Reservoir Characterisation. *Journal of Petroleum Science and Engineering* **31** (2): 113—123.

Rutqvist, J., Rinaldi, A. P., Cappa, F. et al. 2013. Modeling of Fault Reactivation and Induced Seismicity During Hydraulic Fracturing of Shale-Gas Reservoirs. *Journal of Petroleum Science and Engineering* **107**: 31–44.

Schlumberger. 2018. *Petrel E&P Software Platform*, https://www.software.slb.com/products/petrel.

Segall, P. and Lu, S. 2015. Injection-Induced Seismicity: Poroelastic and Earthquake Nucleation Effects. *Journal of Geophysical Research: Solid Earth* **120** (7): 5082—5103.

Stein, R. S. 1999. The Role of Stress Transfer in Earthquake Occurrence. *Nature* **402** (6762): 605—609.

Texas-RRC. 2015. *Commission Called Hearing To Consider Whether Operation Of The XTO Energy, Inc., West Lake Swd, Well No. 1 (Api No. 42-367-34693, Uic Permit No. 12872), In The Newark, East (Barnett Shale) Field, Is Causing Or Contributing To Seismic Activity In The Vicinity Of Reno, Parker County, Texas* (Reprint).

Texas-RRC. H10 Filing System, http://webapps.rrc.state.tx.us/H10/h10PublicMain.do.

USGS. Search Earthquake Catalog, https://earthquake.usgs.gov/earthquakes/search/.

Wang, H. 2000. *Theory of Linear Poroelasticity with Applications to Geomechanics and Hydrogeology*: Princeton University Press.

Yin, J., Park, H. Y., Datta-Gupta, A. et al. 2011. A Hierarchical Streamline-Assisted History Matching Approach with Global and Local Parameter Updates. *Journal of Petroleum Science and Engineering* **80** (1): 116—130.